Adaptive optics optical coherence tomography angiography for morphometric analysis of choriocapillaris [Invited]

KAZUHIRO KUROKAWA,[*] ZHUOLIN LIU, AND DONALD T. MILLER

School of Optometry, Indiana University, Bloomington, IN 47405, USA
[*]*kkurokaw@indiana.edu*

Abstract: Histological studies have shown that morphometric changes at the microscopic level of choriocapillaris (CC) occur with aging and disease onset, and therefore may be sensitive biomarkers of outer retinal health. However, visualizing CC at this level in the living human eye is challenging because its microvascular is tightly interconnected and weakly reflecting. In this study, we address these challenges by developing and validating a method based on adaptive optics optical coherence tomography with angiography (AO-OCTA) that provides the necessary 3D resolution and image contrast to visualize and quantify these microscopic details. The complex network of anastomotic CC capillaries was successfully imaged in nine healthy subjects (26 to 68 years of age) and at seven retinal eccentricities across the macula. Using these images, four fundamental morphometric parameters of CC were characterized: retinal pigment epithelium-to-CC depth separation (17.5 ± 2.1 µm), capillary diameter (17.4 ± 2.3 µm), normalized capillary density (0.53 ± 0.08), and capillary length per unit area (50.4 ± 9.5 mm^{-1}). AO-OCTA results were consistent with histologic studies and, unlike OCTA, showed clear delineation of CC capillaries, a requirement for measuring three of the four morphometric parameters. Success in younger and older eyes establishes a path for testing aging and disease effects in larger populations. To the best of our knowledge, this is the first quantitative morphometry of choriocapillaris at the level of individual capillaries in the living human retina.

References and links

1. R. S. Ramrattan, T. L. van der Schaft, C. M. Mooy, W. C. de Bruijn, P. G. H. Mulder, and P. T. V. M. de Jong, "Morphometric analysis of Bruch's membrane, the choriocapillaris, and the choroid in aging," Invest. Ophthalmol. Vis. Sci. **35**(6), 2857–2864 (1994).
2. C. W. Spraul, G. E. Lang, and H. E. Grossniklaus, "Morphometric analysis of the choroid, Bruch's membrane, and retinal pigment epithelium in eyes with age-related macular degeneration," Invest. Ophthalmol. Vis. Sci. **37**(13), 2724–2735 (1996).
3. C. W. Spraul, G. E. Lang, H. E. Grossniklaus, and G. K. Lang, "Histologic and Morphometric Analysis of the Choroid, BrM and RPE in Postmortem Eyes With AMD and Histologic Examination of Surgically Excised CNV Membranes," Surv. Ophthalmol. **44**, 10–32 (1999).
4. A. Biesemeier, T. Taubitz, S. Julien, E. Yoeruek, and U. Schraermeyer, "Choriocapillaris breakdown precedes retinal degeneration in age-related macular degeneration," Neurobiol. Aging **35**(11), 2562–2573 (2014).
5. D. S. McLeod and G. A. Lutty, "High-resolution histologic analysis of the human choroidal vasculature," Invest. Ophthalmol. Vis. Sci. **35**(11), 3799–3811 (1994).
6. C. W. Spraul, G. E. Lang, G. K. G. E. Lang, and H. E. Grossniklaus, "Morphometric changes of the choriocapillaris and the choroidal vasculature in eyes with advanced glaucomatous changes," Vision Res. **42**(7), 923–932 (2002).
7. S. Dithmar and F. G. Holz, *Fluorescence Angiography in Ophthalmology* (Springer Science & Business Media, 2008).
8. L. A. Yannuzzi, *The Retinal Atlas: Expert Consult - Online and Print, 1e* (Saunders, 2010).
9. I. Grulkowski, I. Gorczynska, M. Szkulmowski, D. Szlag, A. Szkulmowska, R. A. Leitgeb, A. Kowalczyk, and M. Wojtkowski, "Scanning protocols dedicated to smart velocity ranging in spectral OCT," Opt. Express **17**(26), 23736–23754 (2009).
10. R. K. Wang, L. An, P. Francis, and D. J. Wilson, "Depth-resolved imaging of capillary networks in retina and

choroid using ultrahigh sensitive optical microangiography," Opt. Lett. **35**(9), 1467–1469 (2010).

11. S. Makita, F. Jaillon, M. Yamanari, M. Miura, and Y. Yasuno, "Comprehensive in vivo micro-vascular imaging of the human eye by dual-beam-scan Doppler optical coherence angiography," Opt. Express **19**(2), 1271–1283 (2011).

12. C. Blatter, T. Klein, B. Grajciar, T. Schmoll, W. Wieser, R. Andre, R. Huber, and R. A. Leitgeb, "Ultrahigh-speed non-invasive widefield angiography," J. Biomed. Opt. **17**(7), 070505 (2012).

13. R. Motaghiannezam and S. Fraser, "Logarithmic intensity and speckle-based motion contrast methods for human retinal vasculature visualization using swept source optical coherence tomography," Biomed. Opt. Express **3**(3), 503–521 (2012).

14. D. Y. Kim, J. Fingler, R. J. Zawadzki, S. S. Park, L. S. Morse, D. M. Schwartz, S. E. Fraser, and J. S. Werner, "Optical imaging of the chorioretinal vasculature in the living human eye," Proc. Natl. Acad. Sci. U.S.A. **110**(35), 14354–14359 (2013).

15. W. Choi, K. J. Mohler, B. Potsaid, C. D. Lu, J. J. Liu, V. Jayaraman, A. E. Cable, J. S. Duker, R. Huber, and J. G. Fujimoto, "Choriocapillaris and choroidal microvasculature imaging with ultrahigh speed OCT angiography," PLoS One **8**(12), 81499 (2013).

16. B. Braaf, K. V. Vienola, C. K. Sheehy, Q. Yang, K. A. Vermeer, P. Tiruveedhula, D. W. Arathorn, A. Roorda, and J. F. de Boer, "Real-time eye motion correction in phase-resolved OCT angiography with tracking SLO," Biomed. Opt. Express **4**(1), 51–65 (2013).

17. Y. Jia, S. T. Bailey, T. S. Hwang, S. M. McClintic, S. S. Gao, M. E. Pennesi, C. J. Flaxel, A. K. Lauer, D. J. Wilson, J. Hornegger, J. G. Fujimoto, and D. Huang, "Quantitative optical coherence tomography angiography of vascular abnormalities in the living human eye," Proc. Natl. Acad. Sci. U.S.A. **112**(18), E2395–E2402 (2015).

18. O. P. Kocaoglu, S. Lee, R. S. Jonnal, Q. Wang, A. E. Herde, J. C. Derby, W. Gao, and D. T. Miller, "Imaging cone photoreceptors in three dimensions and in time using ultrahigh resolution optical coherence tomography with adaptive optics," Biomed. Opt. Express **2**(4), 748–763 (2011).

19. Z. Liu, O. P. Kocaoglu, T. L. Turner, and D. T. Miller, "Modal content of living human cone photoreceptors," Biomed. Opt. Express **6**(9), 3378–3404 (2015).

20. R. S. Jonnal, O. P. Kocaoglu, Q. Wang, S. Lee, and D. T. Miller, "Phase-sensitive imaging of the outer retina using optical coherence tomography and adaptive optics," Biomed. Opt. Express **3**(1), 104–124 (2012).

21. O. P. Kocaoglu, R. D. Ferguson, R. S. Jonnal, Z. Liu, Q. Wang, D. X. Hammer, and D. T. Miller, "Adaptive optics optical coherence tomography with dynamic retinal tracking," Biomed. Opt. Express **5**(7), 2262–2284 (2014).

22. Z. Liu, O. P. Kocaoglu, and D. T. Miller, "3D Imaging of Retinal Pigment Epithelial Cells in the Living Human Retina," Invest. Ophthalmol. Vis. Sci. **57**(9), 533–543 (2016).

23. O. P. Kocaoglu, Z. Liu, F. Zhang, K. Kurokawa, R. S. Jonnal, and D. T. Miller, "Photoreceptor disc shedding in the living human eye," Biomed. Opt. Express **7**(11), 4554–4568 (2016).

24. S. Makita, K. Kurokawa, Y.-J. Hong, M. Miura, and Y. Yasuno, "Noise-immune complex correlation for optical coherence angiography based on standard and Jones matrix optical coherence tomography," Biomed. Opt. Express **7**(4), 1525–1548 (2016).

25. K. Kurokawa, K. Sasaki, S. Makita, Y.-J. Hong, and Y. Yasuno, "Three-dimensional retinal and choroidal capillary imaging by power Doppler optical coherence angiography with adaptive optics," Opt. Express **20**(20), 22796–22812 (2012).

26. Z. Liu, O. P. Kocaoglu, and D. T. Miller, "In-the-plane design of an off-axis ophthalmic adaptive optics system using toroidal mirrors," Biomed. Opt. Express **4**(12), 3007–3029 (2013).

27. O. P. Kocaoglu, T. L. Turner, Z. Liu, and D. T. Miller, "Adaptive optics optical coherence tomography at 1 MHz," Biomed. Opt. Express **5**(12), 4186–4200 (2014).

28. R. J. Zawadzki, B. Cense, Y. Zhang, S. S. Choi, D. T. Miller, and J. S. Werner, "Ultrahigh-resolution optical coherence tomography with monochromatic and chromatic aberration correction," Opt. Express **16**(11), 8126–8143 (2008).

29. B. A. Shafer, J. E. Kriske, O. P. Kocaoglu, T. L. Turner, Z. Liu, J. J. Lee, and D. T. Miller, "Adaptive-optics optical coherence tomography processing using a graphics processing unit," Conf. Proc. IEEE Eng. Med. Biol. Soc. **2014**, 3877–3880 (2014).

30. M. Mujat, B. H. Park, B. Cense, T. C. Chen, and J. F. de Boer, "Autocalibration of spectral-domain optical coherence tomography spectrometers for in vivo quantitative retinal nerve fiber layer birefringence determination," J. Biomed. Opt. **12**(4), 041205 (2007).

31. American National Standards Institute and Laser Institute of America, *American National Standard for Safe Use of Lasers* (Laser Institute of America, 2014).

32. A. G. Bennett, A. R. Rudnicka, and D. F. Edgar, "Improvements on Littmann's method of determining the size of retinal features by fundus photography," Graefes Arch. Clin. Exp. Ophthalmol. **232**(6), 361–367 (1994).

33. L. An, T. T. Shen, and R. K. Wang, "Using ultrahigh sensitive optical microangiography to achieve comprehensive depth resolved microvasculature mapping for human retina," J. Biomed. Opt. **16**(10), 106013 (2011).

34. D. Y. Kim, J. Fingler, J. S. Werner, D. M. Schwartz, S. E. Fraser, and R. J. Zawadzki, "In vivo volumetric imaging of human retinal circulation with phase-variance optical coherence tomography," Biomed. Opt. Express **2**(6), 1504–1513 (2011).

35. D. J. Moore and G. M. Clover, "The Effect of Age on the Macromolecular Permeability of Human Bruch's

Membrane," Invest. Ophthalmol. Vis. Sci. **42**(12), 2970–2975 (2001).

36. I. Gorczynska, J. V. Migacz, R. J. Zawadzki, A. G. Capps, and J. S. Werner, "Comparison of amplitude-decorrelation, speckle-variance and phase-variance OCT angiography methods for imaging the human retina and choroid," Biomed. Opt. Express **7**(3), 911–942 (2016).

37. A. F. Frangi, W. J. Niessen, K. L. Vincken, and M. A. Viergever, "Multiscale vessel enhancement filtering," Medial Image Comput. Comput. Invervention - MICCAI'98. Lect. Notes Comput. Sci. **1496**(1496), 130–137 (1998).

38. G. Steger, "An unbiased detector of curvilinear structures," IEEE Trans. Pattern Anal. Mach. Intell. **20**(2), 113–125 (1998).

39. T. Wagner and M. Hiner, "ij-ridgedetection: Ridge Detection 1.1.7," Zenodo (2015).

40. J. M. Olver, "Functional anatomy of the choroidal circulation: Methyl methacrylate casting of human choroid," Eye (Lond.) **4**(2), 262–272 (1990).

41. S. Yoneya and M. O. Tso, "Angioarchitecture of the human choroid," Arch. Ophthalmol. **105**(5), 681–687 (1987).

42. M. L. Gabriele, G. Wollstein, H. Ishikawa, L. Kagemann, J. Xu, L. S. Folio, and J. S. Schuman, "Optical Coherence Tomography: History, Current Status, and Laboratory Work," Invest. Ophthalmol. Vis. Sci. **52**(5), 2425–2436 (2011).

43. J. W. Goodman, *Speckle Phenomena in Optics Theory and Applications* (Roberts and Company, 2007).

44. S. Makita, F. Jaillon, I. Jahan, and Y. Yasuno, "Noise statistics of phase-resolved optical coherence tomography imaging: single-and dual-beam-scan Doppler optical coherence tomography," Opt. Express **22**(4), 4830–4848 (2014).

45. A. Moreira, "Improved multilook techniques applied to SAR and SCANSAR imagery," IEEE Trans. Geosci. Remote Sens. **29**(4), 529–534 (1991).

46. B. Park, M. C. Pierce, B. Cense, S.-H. Yun, M. Mujat, G. Tearney, B. Bouma, and J. de Boer, "Real-time fiber-based multi-functional spectral-domain optical coherence tomography at 1.3 microm," Opt. Express **13**(11), 3931–3944 (2005).

47. B. J. Vakoc, G. J. Tearney, and B. E. Bouma, "Statistical Properties of Phase-Decorrelation in Phase-Resolved Doppler Optical Coherence Tomography," Med. Imaging, IEEE **28**(6), 814–821 (2010).

48. B. Cense, W. Gao, J. M. Brown, S. M. Jones, R. S. Jonnal, M. Mujat, B. H. Park, J. F. de Boer, and D. T. Miller, "Retinal imaging with polarization-sensitive optical coherence tomography and adaptive optics," Opt. Express **17**(24), 21634–21651 (2009).

49. C. A. Curcio, J. D. Messinger, K. R. Sloan, A. Mitra, G. McGwin, and R. F. Spaide, "Human chorioretinal layer thicknesses measured in macula-wide, high-resolution histologic sections," Invest. Ophthalmol. Vis. Sci. **52**(7), 3943–3954 (2011).

50. J. J. Weiter, F. C. Delori, G. L. Wing, and K. A. Fitch, "Retinal pigment epithelial lipofuscin and melanin and choroidal melanin in human eyes," Invest. Ophthalmol. Vis. Sci. **27**(2), 145–152 (1986).

51. Q. Wang, S. Chan, J. Y. Yang, B. You, Y. X. Wang, J. B. Jonas, and W. B. Wei, "Vascular Density in Retina and Choriocapillaris as Measured by Optical Coherence Tomography Angiography," Am. J. Ophthalmol. **168**, 95–109 (2016).

52. F. Alten, P. Heiduschka, C. R. Clemens, and N. Eter, "Exploring choriocapillaris under reticular pseudodrusen using OCT-Angiography," Graefes Arch. Clin. Exp. Ophthalmol. **254**(11), 2165–2173 (2016).

53. E. Friedman, T. R. Smith, and T. Kuwabara, "Senile choroidal vascular patterns and drusen," Arch. Ophthalmol. **69**(2), 220–230 (1963).

1. Introduction

The choriocapillaris (CC) is a dense monolayer of interconnecting capillaries that line the inner choroid and is the blood supply for the overlying retinal pigment epithelium (RPE) and photoreceptors. Thus CC is fundamental to maintaining visual function and overall health of the outer retina. Histological studies have shown that morphometric changes at the microscopic level of CC occur with aging [1] and disease such as age-related macular degeneration [2–4], diabetic retinopathy [5] and glaucoma [6], and thus detection and monitoring of changes at this scale provide the greatest promise for improved diagnosis and intervention. However, visualizing and quantifying CC at this level in the living human eye is challenging because the microvascular is tightly interconnected and weakly reflecting.

Traditional methods to enhance contrast of the retinal and choroidal vasculature have been limited to intravenous injection of fluorescein and indocyanine green dyes [7,8]. While a useful clinical tool, the dyes are not specific to CC and can result in adverse patient effects including serious, but rare problems such as anaphylactic shock.

Recently several forms of optical coherence tomography with angiography (OCTA) have been reported that make clever use of blood motion as an intrinsic contrast agent [9–17]. Improved vessel contrast combined with OCT's micron-level axial resolution have allowed

retinal and choroidal vascular to be segmented and visualized noninvasively, including CC [14–17]. Despite this success, however, visualization of the interconnecting capillaries of CC remains prohibitive owing to the lack of lateral resolution to delineate the vessels. This is particularly problematic in the macula where CC vasculature is most dense.

In this study, we address these challenges of image resolution and contrast by developing and validating a method based on adaptive optics optical coherence tomography with angiography (AO-OCTA). For imaging CC, we took advantage of the method's sub-cellular 3D resolution [18,19], sub-cellular 3D registration [20–23], and contrast enhancement of blood flow using an extension of the angiographic method by Makita *et al*. [24]. We improve on the earlier report of AO-OCTA by Kurokawa *et al.* [25] on several technical fronts. These include substantially faster B-scan acquisition, more precise system focus, better AO correction, addition of sub-cellular image registration, and advancements of the angiographic algorithm. Collectively, these resulted in better delineation of CC capillaries and enabled rigorous quantitative morphometry of CC in nine subjects. Compared to OCTA alone, we find AO-OCTA allows a more complete description of CC capillary morphometry and is more consistent with histology. These scientific advances result primarily from the markedly improved capillary clarity afforded by AO. Preliminary results of the morphometric analysis were published in abstract form (Kurokawa K, et al. IOVS 2016;57:ARVO E-Abstract 5915).

2. Methods

Methods is divided into three sections. Section 2.1 describes the Indiana AO-OCT imaging system used in the study. Section 2.2 presents the imaging protocol and experimental procedures along with subject information. Section 2.3 describes post-processing methods necessary for visualizing and quantifying CC along with the correlation analysis as implemented here for OCT angiography.

2.1 The Indiana AO-OCT system

A detailed description of the Indiana AO-OCT system can be found in [26,27]. Briefly, the system is based on a fiber-based Michelson interferometer. The source arm contained a superluminescence diode (BLMD-S-HP3, Superlum, Ireland) with a center wavelength of λc = 790 nm and bandwidth of $\Delta\lambda$ = 42 nm, which provided a nominal axial resolution of 4.7 μm in retinal tissue (n = 1.38) with axial pixel sampling at 0.95 μm/pix. The sample arm consisted of five off-axis afocal telescopes that were constructed from spherical and custom toroidal mirrors, and conjugated the following elements: Shack-Hartmann wavefront sensor to measure ocular monochromatic aberrations, deformable mirror (DM97, ALPAO, France) to correct the measured aberrations, a custom achromatizing lens to correct ocular chromatic aberrations [28], and two galvanometric scanners to perform a 2D raster scan. Lateral resolution was nominally 2.4 μm as defined by 1.22 $\lambda f / d$, where λ is the imaging wavelength (790 nm), f is the equivalent focal length of the eye (16.7 mm), and d is the beam diameter at the eye pupil (6.7 mm). The detection arm was designed for high-speed imaging up to 1 MHz A-scan rates using a 1 × 4 high-speed optical switch that dithered the OCT signal between four identical spectrometers, each with a high-speed Basler Sprint line scan camera. For this study, the inherent sensitivity of OCT angiography to noise necessitated a longer exposure duration than the 500 KHz and 1 MHz A-scan rates we typically operate the system at. We empirically found best performance came with the two-camera mode (see [27] for description of camera modes) acquiring at a 200 KHz A-scan rate with an exposure duration of 5 μsec. This configuration eliminated losses due to camera readout and balanced signal-to-noise ratio (SNR) with image acquisition speed (see Section 4.2 for discussion). To further improve SNR of the CC layer, the AO-OCT coherence gate was positioned immediately behind (posterior of) the retina and CC.

Parallel processing of the raw AO-OCT data on a general purpose graphics processor unit (GPGPU) provided real-time display of the reconstructed volumes, which enabled visual

feedback for eye alignment and focusing [29]. New to this study, we improved the OCT calibration by correcting for spectral-shift and axial-scaling differences between the two spectrometers. This entailed optimizing the common path interference signals generated from two glass slides of different thickness placed in the reference arm. Optimization followed the protocol developed by Mujat, et al. (2007) for calibration of a polarization-sensitive OCT system [30].

2.2 Imaging protocol

Nine healthy subjects with no history of ocular disease were recruited for this study (see Table 1). Average age was 42 years old with a range of 26 to 68 years. All protocols adhered to the tenets of Helsinki declaration and approved by the Institutional Review Board of Indiana University. Written informed consent was obtained after the nature and possible risks were explained. Intensity of the AO-OCT beam was below 430 µW at the cornea and within the safe limits established by the American National Standards Institute (ANSI) [31] for the retinal illumination pattern used and length of the experiment (details below).

One drop of Tropicamide 0.5% was administered to the right eye for mydriasis and partial cycloplegia prior to the imaging session. A dental impression mounted to a motorized XYZ translation stage aligned and stabilized the subject's eye and head to the AO-OCT system. Axial eye length was measured by IOLmaster (Zeiss, Oberkochen, Germany) and used to correct for axial length differences in scaling of the retinal images following the method of Bennett *et al*. [32].

Table 1. Subject information.

Subject ID	Age (years)	Axial eye length (mm)	Gender
A	26	24.04	M
B	27	24.34	M
C	31	23.73	F
D	33	24.68	F
E	36	26.07	M
F	47	23.27	F
G	49	25.40	M
H	61	23.56	M
I	68	24.14	M

For each subject, $1° \times 0.5°$ (h × v) AO-OCT volumes were acquired at seven retinal locations spaced 1° apart along the horizontal meridian from 1° to 7° temporal to fovea. At each retinal location, three AO-OCT videos were acquired at a volume rate of 4.2 Hz with each video containing 20 volumes. The $1° \times 0.5°$ volumes contained 200×200 A-scans (h × v), and therefore sampling along the slow-scan axis (0.5° extent) was two times denser (0.75 µm/A-scan) than along the fast-scan axis (1° extent) (1.5 µm/A-scan). Denser sampling in the slow direction was found empirically necessary for the local correlation analysis between fast B-scans, a fundamental step of our angiographic method (described in Section 2.3.1). Fast B-scans were acquired at a rate of 830 B-scans/s, realized by driving the fast galvanometer with a symmetric triangular waveform as opposed to an MB-scan pattern that is commonly used in conventional OCTA [33,34].

For Subject G, 35 additional volume sets were acquired that tiled a $4° \times 2°$ (h × v) part of the retina centered at 2.5° temporal to fovea. These images were combined to form a relatively wide-field volumetric collage.

Before collection of the AO-OCT volumes, system focus was adjusted to optimize cone photoreceptor image quality, not CC image quality (see Section 4.1 for discussion). This was

determined by visual inspection of cones in *en face* AO-OCT images that were projected axially through the cone inner/outer segment junction (IS/OS) and cone outer segment tip (COST) reflectance bands.

2.3 Post-processing

2.3.1 Selection of images, 3D registration, and reconstruction of intensity and angiographic volumes

To start (Fig. 1 flowchart), intensity and complex volumes were reconstructed. A subset of these were selected that were absent of large apparent motion and had maximal overlap with volumes in the other videos at the same retinal location. Selection included a global correlation analysis to determine those volumes with unacceptable levels of retina motion. This process resulted in the selection of 10 to 22 of the 60 volumes acquired at each retinal location, which increased flow SNR by 3.7 to 8.1 above the baseline (single volume). This SNR improvement was estimated using the empirically determined relation between flow SNR and number of volumes averaged (see appendix).

Critical in our method to visualize and quantify CC was correction of eye motion artifacts in all three dimensions as these can be many times larger than the morphometric parameters we wanted to extract from the volumes. Axial motion was corrected first. We registered each B-scan in the AO-OCT volume using a two-step iterative cross-correlation method. Next, the external limiting membrane (ELM), IS/OS, COST, and RPE layers were identified in each A-scan using an automated algorithm based on multiple one-dimensional cross-correlations [20]. Following axial correction, lateral eye motion was corrected using our stripe-wise registration algorithm that was validated previously for investigations into cone photoreceptor and RPE properties [20–23]. Because all pixels along an A-scan are acquired simultaneously, eye motion is the same along the entire A-scan. Thus, registration of the CC images entailed stripe-wise registration of the projected cone layers (IS/OS + COST) from which registration coordinates were then applied directly to the underlying CC layer. In principle we could have applied the stripe-wise registration directly to CC, but lack of signal and robust image features at this depth made this impractical. The computation time to register images for each retinal location was about an hour.

Parallel to the volume registration, AO-OCTA volume images were generated by applying local correlation analysis to successive pairs of complex B-scans in the selected AO-OCT volumes. We followed the correlation method by Makita *et al.* [24], but extended it to improve performance on AO-OCT data sets with cellular level resolution. Improvements included a more robust bulk motion estimation (step 4 in flowchart), application of registration coordinates (step 5 in flowchart), and use of multiple volume averaging to increase flow SNR (step 6 in flowchart). Details of the correlation analysis are provided in the appendix where the main mathematical expressions are defined and make explicit how we extended the theory and implemented for this study.

Because of the symmetric triangular waveform of the fast galvanometer (previously described), application of the correlation analysis to successive B-scans meant the time interval for the correlation varied from 0.2 to 2.2 msec. Correlations over this time range were sufficient to provide the necessary motion contrast of blood flow in the retinal and choroidal vasculature, but resulted in some variation in contrast depending on the time interval, i.e., the direction of the scan. To correct this variation and increase the flow SNR (defined in Appendix), successive correlation values of the same retinal location and of different time-intervals were averaged. Note that this additional averaging did not reduce spatial resolution as sampling of A-scans along the slow-scan axis was two times denser than along the fast-scan axis. A similar averaging was performed on the corresponding intensity volume.
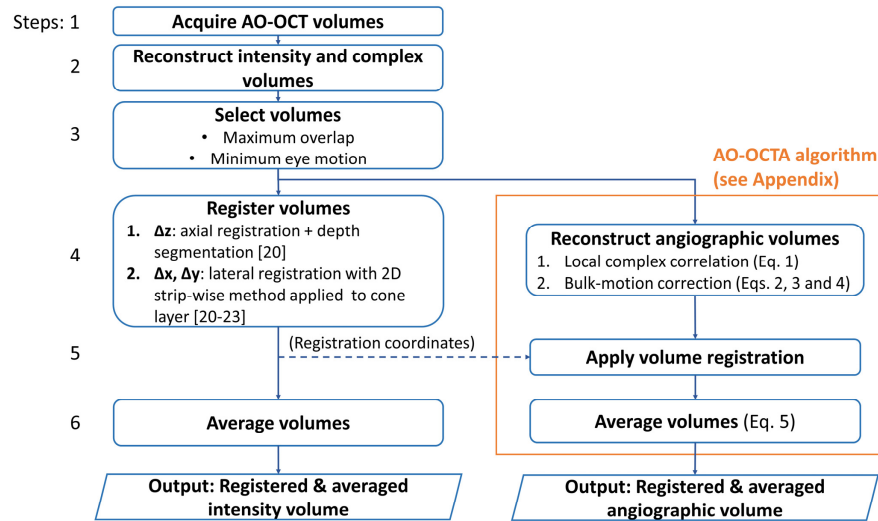
Fig. 1. Flowchart of post-processing steps for reconstructing intensity and angiographic volumes.

2.3.2 Measurement of morphometric parameters

Four morphometric parameters of CC were extracted from the averaged angiographic and intensity AO-OCT images. The four parameters captured key fundamental properties of vessels in CC, namely retinal depth location, *en face* areal coverage, caliper, and length of the capillaries. The first two parameters (depth location and areal coverage) directly impact the efficiency to which oxygen and metabolic exchange occurs between CC and the overlying RPE. As for example, a larger depth separation or a reduced capillary coverage should inhibit (not enhance) physiologic exchange [35]. Areal coverage though is itself defined by two main attributes: capillary caliper and capillary length. Thus quantifying these two additional parameters is necessary to understand source of the coverage, which may have particular importance in the diseased eye for elucidating change, as for example in occlusion or attenuation of capillaries. The four specific morphometric parameters we measured were RPE-to-CC depth separation, normalized capillary density, capillary diameter, and capillary length per area. Each is described below.

RPE-to-CC depth separation was defined as the axial distance between the optical correlates of the RPE and CC layer, both measurable landmarks in our intensity and angiographic AO-OCT images. The RPE correlate was defined at the depth where maximum reflectance occurred posterior of the photoreceptor reflections (IS/OS, COST, and ROST) in the intensity AO-OCT B-scan projection and average A-scan profile. This peak was found by Liu *et al.* [22] to contain the RPE cell mosaic in *en face*. The CC correlate was defined at the depth where maximum angiographic signal occurred posterior of the photoreceptors in the AO-OCTA B-scan projection and average A-scan profile [36]. To improve estimation of the RPE-to-CC depth separation, the axial extent of the local estimation window size, W, in the AO-OCTA image was decreased from 8 pixels (specified in appendix) to 4 pixels. Using these two correlates assured the RPE-to-CC depth separation captured the full thickness of BM's membrane as well as a portion of the basal half of RPE cells and the apical half of CC.

Normalized capillary density was defined as the ratio of lumen area to total area in the *en face* AO-OCTA image of CC. Therefore, a density of '0' indicates no capillaries in the imaged patch and a density of '1' indicates densely packed capillaries with no gaps in between. Lumen area was computed from a binary image of the *en face* AO-OCTA, generated by vessel segmentation based on a multi-scale Hessian filter [37]. Threshold of the

binary image was set such that capillary diameter in the binary image matched that determined for the corresponding morphometric capillary-diameter parameter (described next) of the same capillary.

Capillary diameter was defined as the capillary lumen width as delineated in the *en face* AO-OCTA image. For each retinal eccentricity, a representative capillary was manually selected based on length and visual delineation of the vessel. Using the ridge / line detection algorithm described by Steger [38] and implemented as an ImageJ plugin [39], the capillary center and edges were automatically determined at 44 to 240 (average = 107) points along the vessel extent and from which diameters were extracted. Number of measurement points varied depending on vessel length. Selections of different capillaries in the same AO-OCTA image were found to produce consistent diameters and therefore analysis focused on a single representative capillary per retinal location.

Capillary length per area was defined as the ratio of the total length of capillary vessels in an *en face* AO-OCTA image of CC to the total area of the *en face* image. Total capillary length was obtained by skeletonizing the binary image of the *en face* AO-OCTA followed by counting the remaining white pixels in the skeleton image. Total length was computed as $N + (\sqrt{2} - 1) N_d - 1$, where N is total number of white pixels and N_d is the number of diagonally connected pairs of white pixels.

Measurements of the four morphometric parameters were analyzed across subjects and retinal eccentricities. Because histologic reports of capillary diameter, length, and density at the posterior pole have not shown a retinal eccentricity dependence [40,41], our measurements across retinal eccentricity were sometimes combined to increase statistical power and facilitate comparison to the literature. Age dependence was tested with Spearman's rank correlation. The parameters were also qualitatively analyzed by visual comparison of the AO-OCT intensity and angiographic images, realized for example by constructing *en face* one-to-one fly-through videos of the AO-OCT and AO-OCTA volumes.

3. Results

Vessels of the choriocapillaris were successfully imaged and registered, and morphometric parameters extracted in all nine subjects and seven retinal eccentricities imaged with AO-OCTA.

3.1 Visualizing the choriocapillaris and other cellular structures of the outer retina

The level of cellular detail that can be visualized in the outer retina and choroid based on AO-OCT and AO-OCTA is best appreciated in the 4° × 2° (h × v) volumetric collage on Subject G. Figure 2 shows intensity and angiographic maps of several retina/choroid layers, with selected layers limited to the outer retina and inner choroid where focus is sharp. The location of the AO-OCT collage is denoted in the wide-field SLO image as shown in Fig. 2(a). Figure 2(b) shows a cross sectional view of the retina composed of the superposition of AO-OCT (in grey) and AO-OCTA (in red) B-scan projections. The cross section indicates depth location of IS/OS, COST, rod outer segment tip (ROST), RPE and CC.

The accompanying video of Fig. 2 (Visualization 1) shows the corresponding side-by-side fly-through of the AO-OCT and AO-OCTA volumes. As evident in the figure and visualization, AO-OCTA reveals the exquisite vascular flow pattern in the choriocapillaris bed (Fig. 2(e) and Visualization frames: 40-45), and the coarser pattern of vasculature in the deeper Sattler's layer (Fig. 2(f, g) and Visualization frames: 45-50). Such flow information complements the information provided by AO-OCT intensity, which reveals cellular detail at other layers. For example, the radial striation pattern of Henle's fibers at the interface between ONL and HFL (Fig. 2(c) and Visualization frames: 4-8), and individual photoreceptors at ISOS + COST (Fig. 2(d) and Visualization frames: 22-36). Neither of these cellular-level structures are evident in the AO-OCTA images presumably because these structures are absent of motion, at least over the temporal bandwidth our AO-OCTA was

sensitive to. Note that because AO-OCTA volumes were constructed from the exact same data sets as the AO-OCT intensity volumes, the sharp images of photoreceptors and striation pattern of HFL confirm the high image quality of our AO-OCT data set, whether used to reconstruct intensity or angiographic maps.

Of importance in this study is the CC layer as shown in Fig. 2(e) and Visualization frames: 40-45. While the AO-OCT intensity image shows little to no evidence of CC structure, the AO-OCTA shows striking detail. A regular pattern of blood flow permeates the entire AO-OCTA image and has the distinctive appearance expected of the dense network of anastomosing choriocapillaris in the macula. Visually, the AO-OCTA pattern of motion bears close resemblance to the choriocapillaris vessel pattern in histology (see example in Fig. 3(a)). Based on this and other evidence to follow, we interpret the AO-OCTA motion pattern in the CC layer as the choriocapillaris network of vessels.

Following the binarization procedure detailed in Section 2.3.2, Fig. 3(b) depicts the binary image generated from the AO-OCTA image in Fig. 2(e) with white representing the footprint of CC vessels and black representing the gaps in between. Two morphometric parameters were measured from this binary image. The normalized capillary density was found to be 0.59, and the capillary length per area was 48.5 mm^{-1}. The third morphometric parameter, capillary diameter, was measured at 18.2 ± 6.4 µm using the AO-OCTA image in Fig. 2(e). The fourth morphometric parameter, RPE-to-CC depth separation, was measured at 19.5 ± 2.6 µm using the AO-OCT intensity and angiographic volumes. In addition to these four morphometric parameters, we found the CC pattern to be sufficiently regular that it generated a ring of concentrated power in the two-dimensional power spectrum of the CC image (Fig. 3(c)). The cusp in the power spectrum corresponds to a fundamental spacing of 39 µm, that is, the average spacing between adjacent CC lumens.

Interestingly at deeper layers in the choroid as depicted in Fig. 2(f, g) and Visualization frames 45-50, AO-OCT intensity and angiography show similar resemblance. That is, localized areas of increased reflectance and increased blood flow overlap and likely correspond to branching arterioles and venules that extend inward to feed and drain the choriocapillaris, respectively. This depth in the retina corresponds to Sattler's layer. Figure 4 and Visualization 2 highlight the intricate details of the capillary pattern of CC and provide a better view of the branching hierarchy of blood vessels that evolve from arterioles and venules to the CC capillaries.
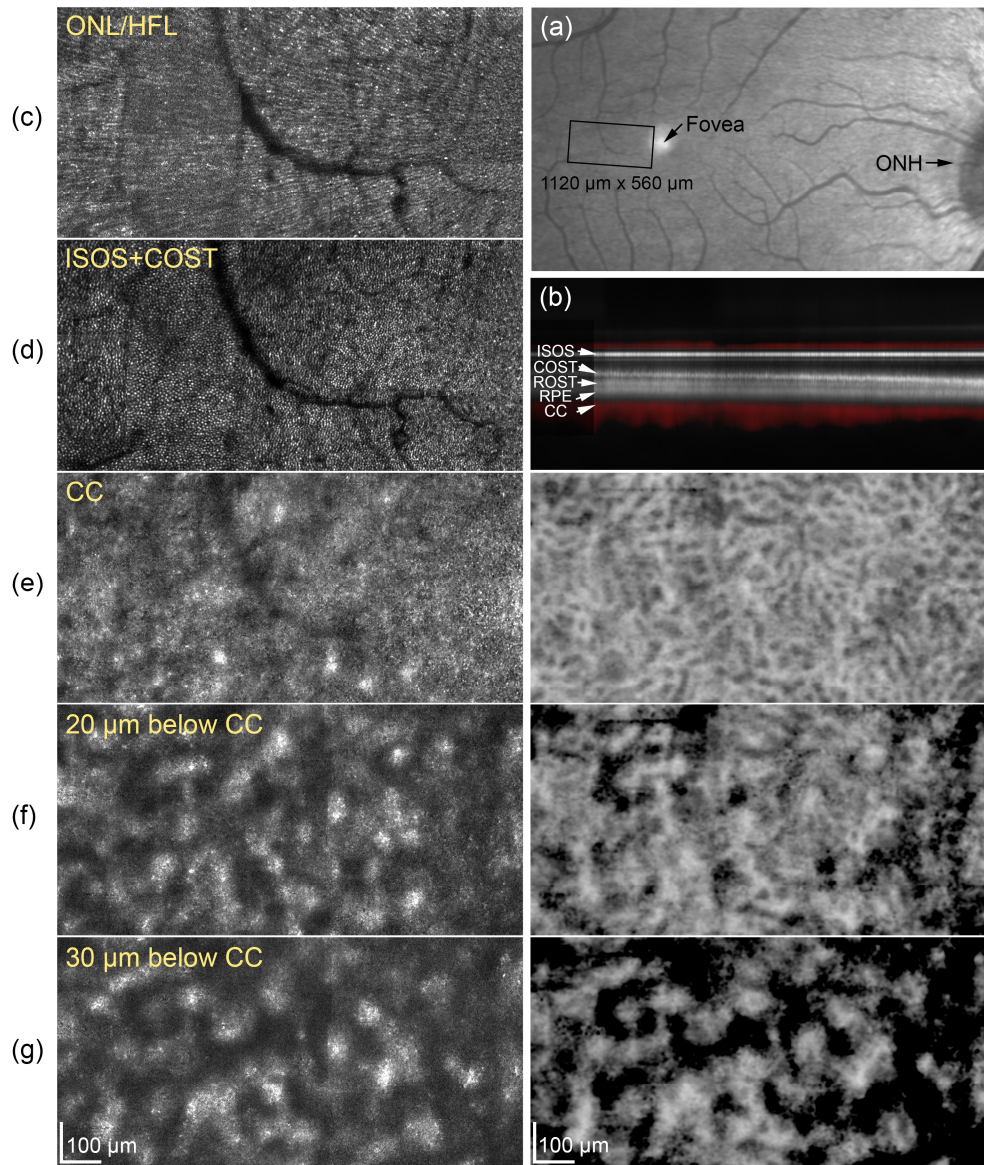
Fig. 2. Comparison of intensity and angiographic maps of the wide-field collage constructed from AO-OCT volumes of the retina and choroid of subject G. (a) Wide-field SLO image from Heidelberg Spectralis denotes location of 4° × 2° AO-OCT collage, (b) The superposition of AO-OCT (in grey) and AO-OCTA (in red) B-scan projections indicate depth location of each band. *En face* images of intensity (left) and angiography (right) are shown extracted from the AO-OCT volume at (c) ONL-HFL interface, (d) IS/OS + COST, (e) CC, (f) 20 μm below CC, and (g) 30 μm below CC. Visualization 1 shows an *en face* side-by-side fly-through of the AO-OCT and AO-OCTA volumes with projected B-scans to mark depth location.
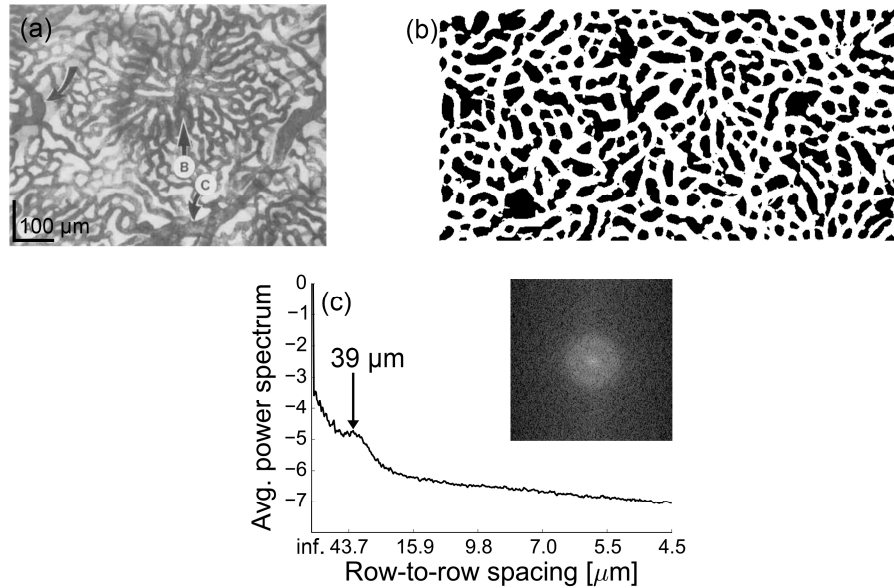
Fig. 3. (a) A representative histologic section of CC at posterior pole of adult human [5] is shown for comparison and scaled to AO-OCTA *en face* images in Fig. 2. (b) Binary image is generated from CC angiographic image in Fig. 2(e) and used to determine normalized capillary density and capillary length per area. (c) Greyscale and circumferential average of two-dimensional power spectrum of CC angiographic image in Fig. 2(e).
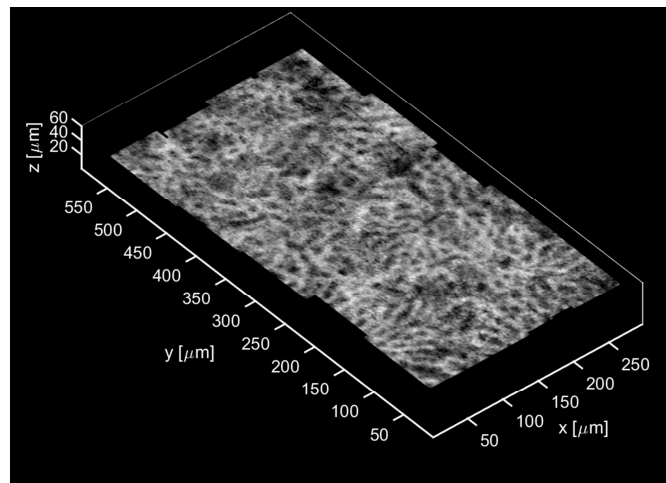

Fig. 4. Perspective view highlights the choriocapillaris bed as extracted from the wide-field AO-OCTA collage of subject G. Corresponding video (Visualization 2) shows fly-through of the AO-OCTA volume and the continuum of vasculature connections between CC and Sattler's layer.

3.2 Quantifying morphometric parameters of the choriocapillaris

Four morphometric parameters were measured in the subjects using 1° × 0.5° AO-OCT volumes. The volumes were notably smaller in extent than the 4° × 2° (h × v) collage shown previously in Figs. 2 and 4, but were more than sufficient for extracting the parameters we sought.

Measurements of RPE-to-CC depth separation are given in Fig. 5. The blue double-headed arrow superimposed on the A-scan profiles of Fig. 5(a) marks the axial separation of the RPE intensity and CC angiographic maxima, which define this parameter. Across the nine subjects and seven retinal eccentricities (see Fig. 5(b)), the RPE-to-CC depth separation was 17.5 ± 2.1 µm (average ± standard deviation). Linear regression indicated a slight increase in separation with age, though the trend was not statistically significant ($r^2 = 0.07$, $P = 0.49$).
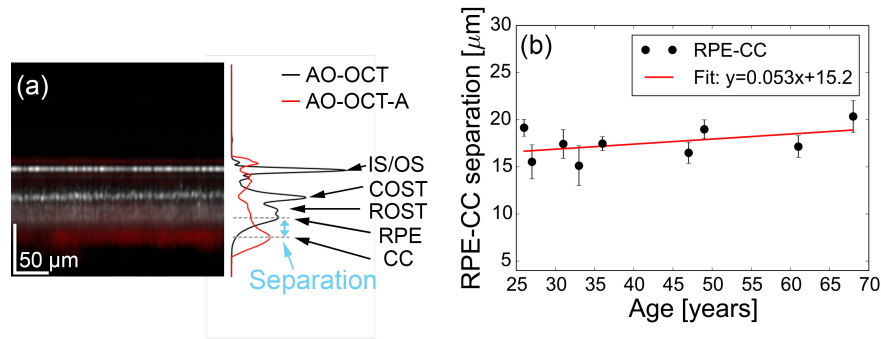

Fig. 5. RPE-to-CC depth separation. (a) Representative AO-OCT intensity (gray scale) and AO-OCTA (red scale) B-scan projections and averaged A-scan profiles are shown superimposed. Volumes were acquired 3° temporal to the fovea of Subject G. (b) RPE-to-CC depth separation for the nine subjects is plotted against age with error bars denoting the standard deviation of measurements across retinal eccentricity. Red line is the linear regression fit.

Figure 6 shows the *en face* AO-OCTA images and corresponding binary images of CC layer for all subjects and retinal eccentricities imaged. Images are displayed on a 9 × 7 (row × column) matrix of age versus retinal eccentricity. Choriocapillaris vessels are evident in all images, though variation in vessel appearance and pattern are apparent. The average capillary diameter across the 63 *en face* AO-OCTA images is 17.4 ± 2.3 µm (average ± standard deviation). Figure 7(a) goes further by plotting capillary diameter as a function of age of the nine subjects. A slight decrease with age is suggested by linear regression although this trend too was not statistically significant ($r^2 = 0.14$, $P = 0.31$).

Computed from the binary images of Fig. 6, the normalized capillary density across subjects and retinal eccentricities (see Fig. 6(b)) was 0.53 ± 0.08 (average ± standard deviation), indicating that a little over half of the CC capillary bed area is occupied by vessel lumen. Linear regression (Fig. 7(b)) indicates this coverage decreases with age from 0.64 for the youngest eye examined to 0.55 for the oldest, though not statistically significant ($r^2 = 0.02$, $P = 0.73$) for the nine eyes in our study.

Finally, the capillary length per CC area is shown in Fig. 8 plotted as a function of age. The capillary length per area across subjects was 50.4 ± 9.5 mm^{-1} (average ± standard deviation), which substantiates the general observation that the vessels exhibit considerable length in the AO-OCTA images.
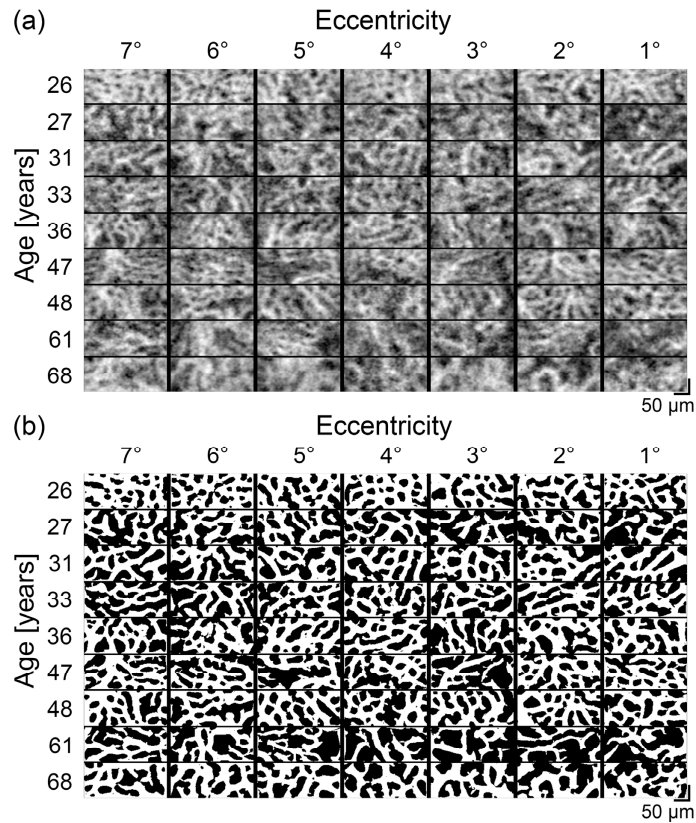
Fig. 6. *En face* AO-OCTA images of CC layer for all subjects and retinal eccentricities imaged. Both (a) angiographic and (b) corresponding binary images are shown with subjects ordered by age.
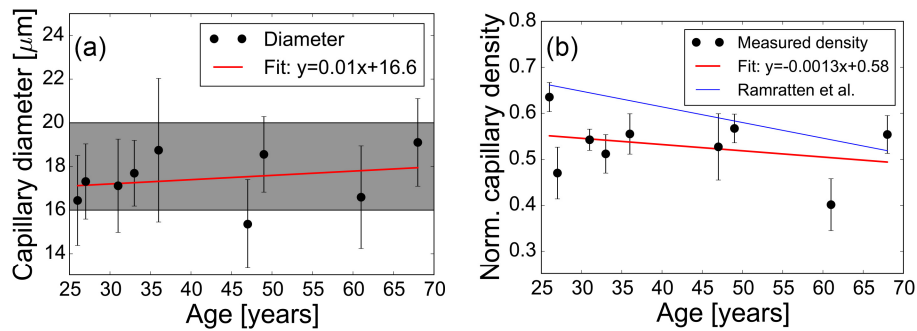

Fig. 7. (a) Capillary diameter and (b) normalized capillary density as a function of age. Error bars denote the standard deviation of measurements across retinal eccentricities. Red lines are the linear regression fits. For comparison in (a), the gray background indicates the capillary diameter range reported in the histologic study of Olver et al. [40]. For comparison in (b), the blue line indicates the linear fit reported in the histologic study by Ramrattan et al. [1].
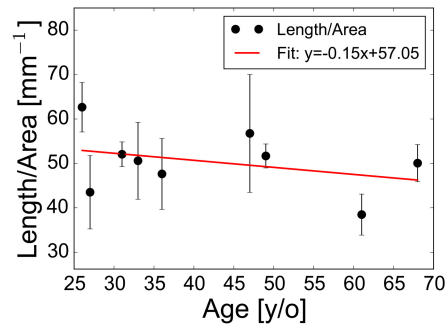
Fig. 8. Average capillary length per *en face* area of CC as a function of age. Error bars denote standard deviation of measurements across retinal eccentricities. Red line is the linear regression fit.

4. Discussion

In this study we developed and validated a method based on AO-OCTA to visualize and quantify the morphometry of capillaries in the choriocapillaris. To do so, we took advantage of the method's sub-cellular 3D resolution provided by AO-OCT, sub-cellular 3D registration provided by custom post-processing algorithms, and contrast enhancement of blood flow realized by OCT angiography. Because our approach obtains intensity and angiographic information from the same acquired AO-OCT volume, the two complementary data sets are automatically mapped one-to-one, which we found helpful in assessing the quality of our measurements and interpreting the layers of the retina.

Two technical points and one application point warrant discussion: (1) balancing AO benefits for CC imaging, (2) determining minimum signal strength for reliable quantitative morphometry of CC, and (3) comparing morphometric parameter values to those in the histologic and *in vivo* imaging literature. For the latter, we find AO-OCTA allows a more complete description of CC capillary morphometry than OCTA alone and is more consistent with histology.

4.1 Balancing benefits of AO in AO-OCTA

AO in ophthalmologic imaging systems is typically used to maximize image sharpness at the retinal layer of interest, realized by placing system focus at the corresponding depth. In this study, we approached the use of AO somewhat differently. Rather than maximize lateral resolution of CC, we instead balanced the benefits of AO across three key performance criteria: resolution of CC vessels, accuracy of *en face* image registration, and angiographic sensitivity to detect CC blood flow.

To achieve this balance, the AO-OCT focus was placed in the photoreceptor layer (not CC) at a depth that maximized cone photoreceptor clarity. Lateral resolution at the photoreceptors was therefore 2.4 μm, the maximum resolution provided by the AO-OCT system (see Methods). Assuming Gaussian beam propagation of the AO-OCT beam from the photoreceptor IS/OS layer to the CC layer, we estimated the lateral resolution at CC layer to be ~4.9 μm. This resolution is less than that at the photoreceptors, but still more than sufficient to resolve the CC vessels, which are of notably larger caliper (17.4 ± 2.3 μm measured in this study). Furthermore, the ~4.9 μm resolution is three to four times better than the 15 to 20 μm resolution often reported for clinical OCT [42].

The main reason to place system focus at the photoreceptor layer was to maximize accuracy of image registration. The cone mosaic, when sharply in focus, provides a strong, stable, high-spatial-frequency signal that results in image registration with subcellular

accuracy [20–23]. Accurate registration to this level benefits AO-OCTA by increasing the effective number of sampling points that can be averaged between volumes resulting in improved flow contrast of the angiographic signal.

Placement of focus at the photoreceptor layer had two important implications for our system's sensitivity to detect CC blood flow. First was the size of the local estimation window for AO-OCTA, a parameter that has opposite influences on the accuracy of the correlation estimation and the effective resolution. Our strategy was to select a window size that both preserved the original ~4.9 µm resolution and increased the accuracy of the correlation estimation. This strategy was possible because of the approximately two times smaller average speckle size (~2.4 µm) compared to the ~4.9 µm lateral resolution at CC. This difference stems from speckle size being, in general, immune to system aberrations, including defocus, and therefore governed by the effects of diffraction [43]. Because of this, we selected a small local estimation window with a size of 5.8 µm × 7.6 µm (lateral × depth). In this way the 5.8 µm lateral dimension was comparable in size to the lateral resolution at CC (~4.9 µm) and more than two times larger than the average speckle size (~2.4 µm). The latter increased the estimation accuracy, which depends on the effective number of independent samples within the window [44,45].

The second important implication is that the smaller beam size of AO-OCTA (~4.9 µm) compared to clinical OCT (15 to 20 µm) provides greater sensitivity to small displacements generated by blood flow. The actual improvement depends on the fractional displacement given as the ratio of the fast B-scan separation (0.75 µm) to the beam spot size (~4.9 µm) [44,46,47]. This sensitivity is further improved by the two-times smaller speckle size. Note however that the sensitivity gain is not confined to the signal (blood motion), but any motion including bulk motion of the retina, e.g., eye movement. We successfully reduced influence of this unwanted motion by acquiring fast B-scans at a high rate (830 B-scans/s) and densely spaced (0.75 µm), post processing to handle the symmetric triangular scan pattern, and correction factors given by Eqs. (2) and (4). We found empirically a ratio of (B-scan separation / beam spot size = 0.75 µm / 4.9 µm =) 0.15 worked best, resulting in fine sampling of CC layer without significant motion artifacts, while maintaining high sensitivity to small displacements in blood cells.

4.2 Signal strength in AO-OCTA

Repeatable and accurate quantitative measurements with AO-OCTA require sufficient signal from the tissue being examined, in our case the choriocapillaris bed. To determine the minimum signal strength necessary for reliable CC imaging, we analyzed one of our morphometric parameters, normalized capillary density, as a function of SNR that was realized by generating different levels of noise in the images. SNR was defined as $10\log(I/N)$, where I is the maximum intensity in the AO-OCT volume or CC layer, and N is the variance of the noise. N was measured in the vitreous where noise dominated signal. The maximum SNR using peak intensity in the volume and averaged across the nine subjects was 35.9 ± 1.8 dB (see Fig. 9(a)). Even though the AO-OCT exposure duration was only 5 µs, the resulting SNR of 35.9 dB is approximately 6 dB better than that typically observed with clinical OCT images (~30 dB). Based on an earlier study in which we measured the dynamic range benefit of AO [48], we attribute the 6 dB gain primarily to the AO.

The maximum SNR using peak intensity in CC layer and averaged across the nine subjects was much less, being 20.7 ± 1.4 dB. This value is almost 16 dB below the maximum SNR in the same volumes (35.9 dB) and underscores the challenge of imaging this dim layer that is masked by the overlying retina. We determined the minimum signal strength necessary for reliable measurement of CC by numerically adding complex circular Gaussian noise to the AO-OCT data to systematically control SNR from approximately 10 to 20 dB, and then from which computed *en face* AO-OCTA images. A representative set of example images on subject A at 6° retinal eccentricity is given in the top row of Fig. 9(b). Binary images (bottom

row of Fig. 9(b)) were generated from these images and from which normalized capillary densities were extracted and plotted as a function of SNR (Fig. 9(c)) for that subject. Figure 9(c) also plots the results of the other eight subjects at the same retinal eccentricity.

The AO-OCTA images of Fig. 9(b) show qualitatively that capillary clarity is stable at high SNR, but degrades notably at the lowest SNR levels that we examined. This visual trend is quantified in the normalized capillary density plot (Fig. 9(c)) that shows a monotonic increase in density with SNR that approaches an asymptote, which for the polynomial fit (solid black line) is about 0.5. In general, an SNR below 14 dB yielded *en face* AO-OCTA images of susceptible capillary quality and capillary densities that trended notably downward from the asymptotic limit. In contrast, capillary density measurements with SNRs of at least 16 dB varied by no more than 10%, indicating measurements over this SNR range (> 16 dB) reliably quantified CC. Using this interpretation, more than 99% (± 3 standard deviations) of the CC SNR measurements (20.7 ± 1.4 dB) fell in this range, substantiating the claim of reliable morphometric measurements for the eyes we examined.
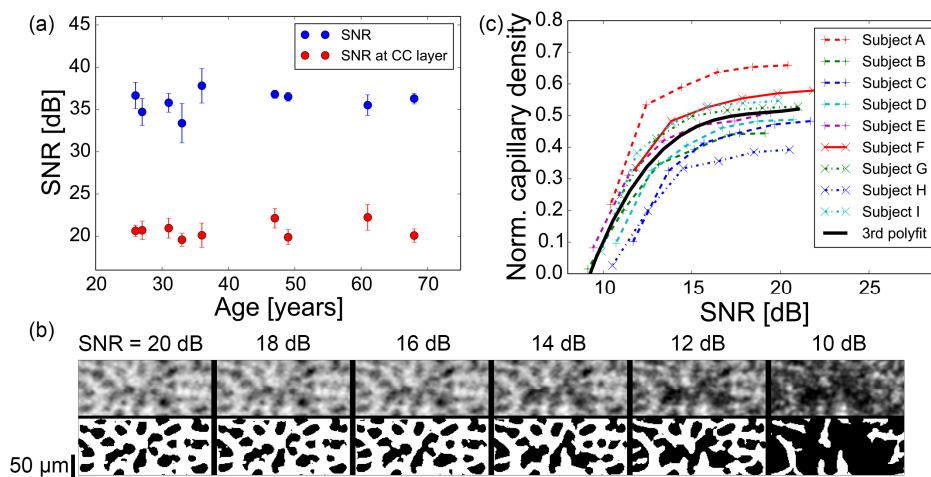

Fig. 9. (a) Maximum SNR in the volume and CC layer are plotted as a function of age. Error bar denotes the standard deviation across retinal eccentricities. (b) The *en face* AO-OCT images (first row) and binary images (second row) of Subject A at 6° retinal eccentricity at different SNR. (c) The normalized capillary density of all subjects at 6° retinal eccentricity is plotted as a function of SNR. Black solid line is a 3rd-order polynomial fit to the subject data.

Note that the AO-OCTA signal sometimes appeared elevated immediately above IS/OS layer, which is most evident when viewed in cross section, as for example Figs. 2(b) and 5(a). This apparent elevation, however, is an artifact of the sidelobes of the axial point spread function. The artifact shows around IS/OS as the IS/OS reflection is the strongest in our images and highly localized (see A-line traces in Fig. 5). Subsequent to our study, we were able to minimize this sidelobe artifact with proper correction of polarization mode dispersion in the SLD isolator. The correction, however, resulted in the same quality of AO-OCTA images of CC and had no effect on our analysis of the CC morphometric parameters. It was therefore not used in this study.

4.3 Comparison of measured morphometric parameters to other CC studies

We characterized the choriocapillaris in the macula by quantifying four morphometric parameters: RPE-to-CC depth separation (Fig. 5), capillary diameter (Fig. 7(a)), normalized capillary density (Fig. 7(b)), and capillary length per area (Fig. 8). It is difficult to compare these measurements to histologic and other *in vivo* studies owing to differences between subjects, retinal locations, and age. Additional differences arise in comparing to histologic studies due to uncertainties in tissue shrinkage and uncertainties in the optical attributes of the

cellular morphology. However a few notable comparisons with reported measurements in the macula are made here for each morphometric parameter.

The RPE-to-CC depth separation is the axial distance between the RPE and CC peak reflections and thus represents a composite of RPE, BM and CC. Our measurements show that the RPE-to-CC depth separation averaged across subjects and retinal eccentricities was 17.5 ± 2.1 µm (Fig. 5). To compare with histologic measurements in the macula, we approximated this separation as the sum of one half of RPE thickness, full BM thickness, and one half CC thickness. Using this interpretation, the measurements by Spraul *et al.* [2] on 40 eyes (age: 82.4 ± 7.2 years) and Curcio *et al.* [49] on 18 eyes (age: 67.7 ± 16.0 years), yielded RPE-to-CC depth separations of 12.1 µm and 13.5 µm, respectively. A third histologic study by Ramrattan *et al.* [1] using 95 eyes (age range 6 to 100 years) yielded 12.9 µm for an age matched (42 years old) subject, that is, the average subject age in our study. However, because Ramrattan et al. did not measure RPE thickness, we estimated it at 11.0 µm based on the average thickness from three other histologic studies [2,49,50]. Our thickness measurement of 17.5 µm is greater than all three histologic studies. But the difference (average of 5 µm) is likely within the uncertainties attributable to anatomical interpretation of the reflectance peaks in the RPE and CC layers of our AO-OCT intensity and angiographic images, and to a lesser extent tissue shrinkage in histology.

To the best of our knowledge there is no *in vivo* imaging study that has evaluated the separation between RPE and CC as we have done here, even though numerous studies have demonstrated choriocapillaris imaging with OCTA [14–17,51,52]. Three of these studies segmented immediately below RPE, but did not specify the depth [15–17]. Wang *et al.* [51] using 105 normal eyes (age: 35.9 ± 13.8 years) and Alten *et al.* [52] using 40 normal eyes (age: 69.53 ± 11.13) reported segmenting at a RPE-to-CC depth separation of 30 µm or more, which is two to three times deeper below the retina than our measurements and that of the histologic studies. Finally, Kim *et al.* [14] reported a CC segmentation depth of ~5.2 µm below BM (not RPE) in one healthy subject at 6° nasal retinal eccentricity. To compare to this latter study, we identified the BM depth peak position in two of the younger subjects (Subject A and C; not shown), an observation consistent with what we had reported previously in an earlier AO-OCT study [22]. Using this identification, the BM-to-CC depth separation of these two eyes was 9.0 ± 0.5 µm, which on average is 3.8 µm thicker than that in the Kim *et al* subject.

We were particularly interested in measuring the normalized capillary density as this parameter directly relates to the apical surface area of CC, where oxygen and metabolic exchange with the RPE occurs. Using AO-OCT, we found the normalized capillary density averaged across subjects and retinal eccentricities was 0.53 ± 0.08. The histologic study of Ramrattan *et al.* [1] on 95 eyes reported an age matched (42 years old) density of 0.61, which is 13% higher than ours. This difference could be caused simply by differences in definition of the capillary lumen boundary. While histology measures the actual anatomical boundary of the inner endothelial wall, AO-OCTA measures the boundary location based on blood flow in the CC lumen. As flow must converge to zero at the wall boundary, AO-OCTA may underestimate the lumen diameter and therefore the normalized capillary density. Regardless of this difference, a virtue of the flow metric is that it detects only perfused, functioning capillaries and therefore measures what could be called a functioning capillary density as opposed to what histology measures, which is a structural capillary density that cannot distinguish between perfused and non-perfused vessels. It is important to note that similar measurement variations also exist between the histologic studies. For example, Spraul *et al.* [2] reported a normalized capillary density of 0.51 ± 0.08 in 40 eyes with an average age of 82.4 ± 7.2 years, For this age (82.4 years old), Ramrattan *et al.* [1] found a density of 0.47, which is 7.9% smaller than that of Spraul *et al.* and approaching the 13% difference between our study and Ramrattan's.

As for *in vivo* imaging studies of normalized capillary density, we found two that used commercial OCTA systems [51,52], though results varied widely. Average normalized capillary density from Wang *et al.* [51] was 0.445 among 105 healthy subjects (age: 35.9 ± 13.8 years) and from Alten *et al.* [52] was 0.99 among 40 subjects (age: 69.53 ± 11.13). Direct comparison of these two suggests normalized capillary density must increase dramatically with age, but this conflicts with histologic studies that show a decrease (not increase) with age.

Our measurements of capillary diameter averaged across subjects and retinal eccentricities was 17.4 ± 2.3 μm. This value is consistent with histologic measurements, though reports are sparse. Olver [40] reported a diameter range of 16 to 20 μm for the posterior pole of one eye and Friedman *et al.* [53] reported an average diameter of 15 μm (with no other statistic information provided) for the posterior pole in 105 eyes. Two *in vivo* imaging studies reported higher values. Kim *et al.* [14] reported an approximate capillary diameter of ~20 μm in one healthy subject at 6° nasal retinal eccentricity. Wang *et al.* [51] showed a diameter of 22.1 ± 0.7 μm among 105 normal subjects. Our study is more consistent with the smaller diameters reported with histology than with OCTA, likely because the reduced blurring afforded by AO provides a truer (smaller) diameter estimate. In support, visual inspection of our AO-OCTA images (e.g., Figs. 2, 4, and 6) showed clear delineation of CC vessels compared to OCTA images in the literature [14–17,51,52].

Finally, we were unable to compare our measurements of capillary length per area to either histology or other *in vivo* imaging studies as we found no data in the literature to compare. This surprised us given the fundamental importance of this metric. However, we suspect this is primarily because of the lack of sufficient vessel clarity using other *in vivo* imaging methods. Indeed, from our visual inspection of OCTA images in the literature, we concluded a reliable vessel length metric for CC would be unlikely to extract. As for histology, many of the studies analyzed the retina in cross section, a view that does not lend itself to metrics, such as this one, that require an *en face* view of the choriocapillaris bed.

Capillary length per area is a fundamentally important metric as it along with capillary diameter are the two main attributes of CC capillary coverage (defined here as normalized capillary density) and thus to understand coverage requires understanding the contributions of capillary length and diameter. To assess their influence (plots not shown), we first plotted capillary length per area versus capillary coverage, i.e., plotting the measurements in Fig. 8 against those in Fig. 7(b). Linear regression gave a coefficient of determination (R^2) value of 0.76 indicating a strong correlation between these two morphometric parameters. However, an even larger R^2 value (0.94) was obtained by including the influence of capillary diameter by plotting the multiplication of capillary length per area with capillary diameter versus capillary coverage. For this comparison, capillary diameter measurements were obtained from Fig. 7(a). Based on this analysis, we conclude that, at least in the normal eyes examined, capillary length per area is a strong predictor of capillary coverage, but an even stronger predictor is when capillary diameter is included.

It will be interesting how these predictors play out in the diseased eye where capillaries can change in length (as for example by occlusion, dropout, and angiogenesis) or diameter (attenuation and thickening) depending on the disease. This remains future work.

4.4 Influence of aging on morphometric parameters

We tested the four morphometric parameters for an age dependence across the age range examined (26 to 68 years). Regression lines in Figs. 5, 7(b) and 8 show that with age RPE-CC separation increases, and normalized capillary density and capillary length per area decrease. These trends, while not statistically significant (P>0.05), do match histology [1]. The fourth morphometric parameter, capillary diameter, slightly increased with age though was not statistically significant (P>0.05), and we found no literature to test against. Interestingly, histologic measurements reported for the capillary diameter in the axial dimension (as

opposed to the lateral dimension that we measured) showed a decrease in diameter with age [1]. While we can only speculate, perhaps preservation of the lateral dimension of CC vessels is more vital for maintaining proper diffusion of oxygen and nutrients across the fenestrated apical surface of the vessels as opposed to the axial dimension of the vessel. This requires further investigation.

The statistical power of just nine subjects used in the present study is obviously limited, but the fact that we have demonstrated that four fundamental morphometric parameters of CC vessels are measureable in younger and older eyes establishes a clear path for testing aging and disease effects in a larger population.

5. Conclusion

We have successfully developed and validated a method based on AO-OCTA to visualize and quantify the morphometry of individual capillaries in the choriocapillaris. AO-OCTA has captured, to the best of our knowledge, the sharpest images to date of the individual vessels that compose the CC capillary bed. Using this technology, we quantified the morphometry of CC vessels at 63 different retinal locations in nine eyes that covered a wide age range. We found AO-OCTA allows a more complete description of CC capillary morphometry than previous reports with OCTA alone and is more consistent with histology.

Appendix: Noise-immune complex correlation map

The local correlation analysis consisted of three steps: (1) compute local correlation coefficient between complex B-scans of AO-OCT volume, (2) remove bulk motion, and (3) repeat steps one and two on additional volumes of the same retinal patch and then average to improve the flow SNR. To start, the complex correlation coefficient was computed within a local estimation window that centered on each pixel in the AO-OCT B-scans as defined by

$$\rho_f(x,z) = \frac{\left|C_f(x,z)\right|}{\sqrt{S_f(x,z)\,S_{f+1}(x,z)}}, \tag{1}$$

where $C_f(x,z)$ is the covariance between successive B-scan images and defined as $C_f(x,z) = \sum_\xi \sum_\zeta g_f^*(x+\xi, z+\zeta) \cdot g_{f+1}(x+\xi, z+\zeta)$, and $S_f(x,z)$ is the signal strength that is defined as $S_f(x,z) = \sum_\xi \sum_\zeta \left(\left| g_f(x+\xi, z+\zeta) \right|^2 - N \right)$. In these two expressions, g_f is the complex B-scan image with subscript f denoting the B-scan frame index of the volume, ξ and ζ are the lateral and axial pixel coordinates of the local estimation window centered at (x,z), the superscript $*$ represents the complex conjugate, and N is the noise power estimated in the vitreous portion of the B-scan where there is effectively no signal. Subtracting N removes the bias caused by random noise [44]. The local estimation window size was set at 4 pixel × 8 pixel (lateral × depth), which is equivalent to 5.8 μm × 7.6 μm in retinal tissue. This size was empirically found to contain enough pixels to accurately estimate the correlation, while small enough to minimize spatial blur (see Section 4.1 for discussion).

Next, the bulk motion was estimated and corrected using the bulk-phase offset, $\Delta\varphi_{bulk}(x)$, and reduced correlation coefficient, $\rho_{bulk}(x)$. Here we assumed that bulk-motion (1) occurred on a time scale much slower than that of blood cells in the retinal and choroidal vasculature and (2) was invariant across the local estimation window and along the entire A-scan. The bulk-phase offset was estimated for each A-scan using

$$\Delta\varphi_{bulk,f}(x) = \arg\left(\sum_z C_f(x,z) \right), \tag{2}$$

where the z summation is over the A-scan length. Thus, the complex correlation coefficient with bulk-phase correction is given by

$$\overline{\rho_f}\left(x,z\right) = \frac{\left| C_f\left(x,z\right) \cdot e^{\left(-i\Delta\varphi_{bulk,f}\left(x\right)\right)} \right|}{\sqrt{S_f\left(x,z\right)S_{f+1}\left(x,z\right)}}. \tag{3}$$

The reduced correlation coefficient was estimated by determining the maximum covariance, (as opposed to the maximum correlation as in [24]), in each A-scan using

$$\rho_{bulk,f}\left(x\right) = \overline{\rho_f}\left(x, \arg\max_z \left| C_f\left(x,z\right) \right|\right). \tag{4}$$

Maximum covariance was used as it accounts for variation in signal strength and therefore provides a more robust estimate of the correlation coefficient of static tissue (no motion). Furthermore, Eq. (4) corrects for bulk motion errors generated by the symmetric scan and dense sampling. These are errors whose correction has not been previously reported.

Finally, to increase flow SNR, multiple registered volumes of the same retinal patch were averaged. This averaging has the same SNR effect as averaging different polarization images as done by Makita *et al.* [24] and is expressed as

$$\rho_f'\left(x,z\right) = \frac{\sum\limits_m \left| C_f\left(x,z\right) \cdot e^{\left(-i\Delta\varphi_{bulk,f}\left(x\right)\right)} \rho_{bulk,f,m}^{-1}\left(x\right) \right|}{\sum\limits_m \varepsilon_{f,m}\left(x,z\right)\sqrt{S_{f,m}\left(x,z\right)S_{f+1,m}\left(x,z\right)}}, \tag{5}$$

where m is the volume index, and ε is a weighting factor that accounts for low signal SNR and defined as $\varepsilon\left(x,z\right) = 0.5\left[\operatorname{sgn}\left(S_{f,m}\left(x,z\right)\right) + \operatorname{sgn}\left(S_{f+1,m}\left(x,z\right)\right)\right]$ [24]. It is important to note that motion between volumes was corrected by the 3D registration as described previously, and therefore only highly correlated frames from other volumes were averaged in this step. Averaging in this way reduced the estimation noise that we then quantified in terms of flow SNR. We defined flow SNR as the ratio of mean decorrelation value at CC layer to standard deviation at RPE layer. The RPE reflectance was selected as it is stable relative to blood flow, strong, and approximates fully developed speckle. Using this definition, we empirically found flow SNR to increase linearly with number of volumes averaged with a slope of 0.37.